Reversible Thermochromism and Strong Ferromagnetism in Two-Dimensional Hybrid Perovskites

Bing Sun, Xiao-Fei Liu, Xiang-Yang Li, Yang Cao, Ze Yan, Lin Fu, Nujiang Tang, Qiang Wang, Xiangfeng Shao, Dezheng Yang,* and Hao-Li Zhang*

Abstract: Two-dimensional (2D) hybrid perovskites have shown many attractive properties associated with their soft lattices and multiple quantum well structure. Herein, we report the synthesis and characterization of two new multifunctional 2D hybrid perovskites, $(PED)CuCl_4$ and $(BED)_2CuCl_6$, which show reversible thermochromic behavior, dramatic temperature-dependent conductivity change, and strong ferromagnetism. Upon temperature change, the $(PED)CuCl_4$ and $(BED)_2CuCl_6$ crystals exhibit a reversible color change between yellow and red-brown. The associated structural changes were monitored by in situ temperature-dependent powder X-ray diffraction (PXRD). The $(BED)_2CuCl_6$ exhibits superior thermal stability, with a thermochromic working temperature up to 443 K. The conductivity of $(BED)_2CuCl_6$ changes over six orders of magnitude upon temperature change. The 2D perovskites exhibit ferromagnetic properties with Curie temperatures around 13 K.

Organic–inorganic hybrid halide perovskite materials have emerged as a new class of remarkable semiconductors for high-performance optoelectronics.[1–6] The majority of current research in this area is based on three-dimensional (3D) perovskite structures, which have a general formula of ABX_3, where A is monovalent cation, B is divalent metal cation, and X is halide.[7] Slicing of 3D perovskite lattice along (100),

(110), (111) crystallographic planes with the elimination of the octahedra lying in the slicing plane lead to common two-dimensional (2D) perovskites with single-octahedra or thicker slabs.[8] Lowering the dimensionality to 2D with corner-sharing octahedral layers and bulky organic cations separating perovskite layers gives rise to increased structural diversity and new functionalities.[9–11] Besides, 2D hybrid perovskites have attracted much attention as alternative photovoltaic materials because of an improved stability arising from hydrophobic interactions, which block moisture diffusion in the material.[12–14] In 2D perovskites, there is no Goldschmidt's tolerance factor restriction.[15] As a result, the optical and electronic properties of the materials can be tuned not only by metal cation and halide anion but also organic molecules with different sizes and functional groups, providing almost unlimited compositional and structural versatility. Given the vast design space for both organic and inorganic components, more "exotic" functions have also been envisioned with 2D hybrid perovskites, including singlet fission, room-temperature phosphorescence and third harmonic generation.[16–19]

In stark contrast to conventional optoelectronic materials such as Si and GaAs, hybrid halide perovskites are structurally softer due to weaker electrostatic interaction between the lattice ions.[20,21] Such structural "softness" results in a highly reconfigurable crystal structure with relatively easy structural rearrangements to undergo a rich variety of solid-solid phase transitions under external stimuli.[22] We have observed pressure-induced changes in photoluminescence and conductivity in several hybrid halide perovskites, all of which involved structural transformation.[23–26] Beside optoelectronic properties, the color appearance can also change significantly during phase transitions in 3D hybrid perovskites. For example, dihydrated methylammonium lead iodide was found to exhibit highly reproducible and reversible thermochromic properties upon phase transformation.[27] However, thermochromic characteristics are rarely reported on 2D hybrid perovskite, remaining an interesting yet underexplored research field.

2D layered perovskite possesses multiple-quantum-wells (MQW) structure, with alternating octahedra network layers and organic molecule layers.[28] The inorganic slabs serve as the potential wells while the organic layers function as the potential barriers. The band gap of each quantum-well is mainly determined by the number of inorganic monolayer sheets within a layered perovskite.[29] The MQW electronic structure enables 2D halide perovskite particularly interesting for optoelectronic applications and magnetic studies.[30] Magnetic susceptibility was investigated in

[*] B. Sun, X. F. Liu, X. Y. Li, Prof. Q. Wang, Prof. X. Shao,
Prof. H. L. Zhang
State Key Laboratory of Applied Organic Chemistry, Key Laboratory of Special Function Materials and Structure Design, College of Chemistry and Chemical Engineering, Lanzhou University
Lanzhou 730000 (P. R. China)
E-mail: haoli.zhang@lzu.edu.cn

Y. Cao, Z. Yan, Prof. D. Yang
Key Laboratory for Magnetism and Magnetic Materials of Ministry of Education, School of Physical Science and Technology
Lanzhou University
Lanzhou 730000 (P. R. China)
E-mail: yangdzh@lzu.edu.cn

L. Fu, Prof. N. Tang
National Laboratory of Solid State Microstructures & Collaborative Innovation Center of Advanced Microstructures, School of Physics
Nanjing University
Nanjing 210093 (P. R. China)

Prof. H. L. Zhang
Tianjin Key Laboratory of Molecular Optoelectronic Sciences
Collaborative Innovation Center of Chemical Science and Engineering, Tianjin 300072 (P. R. China)

Supporting information and the ORCID identification number(s) for the author(s) of this article can be found under:
https://doi.org/10.1002/anie.201910701.

$Cs_4Mn_{1-x}Cu_xSb_2Cl_{12}$ ($x = 0–1$), which were dependent on the concentration of manganese and copper.[31] Investigations on the spin-reorientation and spin-control in 2D hybrid perovskite may help to design new materials for future spintronics.[32,33] Despite extensive investigations on perovskites, ferromagnets coupled with thermochromism has not been reported to date.

As discussed above, the rich structural diversity and "softness" in lattice structures make 2D perovskite an ideal platform for the design of novel functional materials. Chemical tuning of the organic spacer cations and metal ions may enable the integration of multiple properties into 2D hybrid perovskites. Herein, for the first time, we report the design and synthesis of ferromagnetic 2D hybrid perovskite with thermochromic properties. We prepared two new 2D hybrid perovskites, $(PED)CuCl_4$ (PED = *N*-phenylethylene-diamine) and $(BED)_2CuCl_6$ (BED = *N*-benzylethylenedia-mine), which exhibit reversible thermochromic properties attributed to changes in crystal structure upon temperature variation. Temperature-dependent conductivity experiments revealed that the conductivity change of the $(BED)_2CuCl_6$ spans nearly six orders of magnitude. In addition, these 2D perovskites are ferromagnet with Curie temperatures about 13 K. Integration of multiple stimuli-response properties into 2D hybrid perovskites shall significantly broaden their applications.

Single crystals were synthesized from a solution of cupric chloride dihydrate and ammonium salt followed by cooling of the solution to room temperature. Detailed synthesis procedures are provided in the Supporting Information. The crystal structures of the $(PED)CuCl_4$ and $(BED)_2CuCl_6$ are illustrated in Figure 1, and the crystal data and structure refinement are summarized in Table S1 and Table S2 in the Supporting Information. Molecular structures of the organic cations used in this work are shown inset of Figure 1. The powder X-ray diffraction (PXRD) patterns of the crystals show almost identical features as simulated spectra based on their single crystal structures (Figure S1), confirming the pure phase of $(PED)CuCl_4$ and $(BED)_2CuCl_6$. Thermogravimetric analysis (TGA) measurements indicate that $(BED)_2CuCl_6$ possesses high thermal stability, with decomposition temper-

ature above 478 K (Figure S2). In contrast, the $(PED)CuCl_4$ shows a moderate thermal decomposition temperature of 393 K. Single crystal X-ray diffraction (SCXRD) data reveals that both $(PED)CuCl_4$ and $(BED)_2CuCl_6$ have a 2D layered structure, in which the inorganic sheets are formed by corner-sharing copper chloride octahedral, while the successive inorganic sheets are interleaved by organic ammonium salt. The $(PED)CuCl_4$ crystallizes in the monoclinic system $P2_1/c$ space group, with a primitive unit cell of dimensions (150 K) $a = 15.3542(7)$, $b = 7.4336(3)$ and $c = 12.1823(6)$. $(BED)_2CuCl_6$ crystallizes in the orthorhombic system *Pbca* space group, with a primitive unit cell of dimensions (150 K) $a = 7.2375(3)$, $b = 7.2382(3)$ and $c = 48.029(5)$. Due to the Jahn–Teller effect, which is common in Cu^{2+}-based complexes,[34] the octahedra in the inorganic sheet are distorted. The perovskite $(PED)CuCl_4$ consists of corrugated copper-chloride sheets. When the PED is replaced by a longer amine BED, the corrugated layers in the $(BED)_2CuCl_6$ can no longer form, and the $(BED)_2CuCl_6$ has flat copper-chloride sheets, suggesting that the formation of the corrugated sheets is cation dependent. Such cation-depend change of inorganic sheet pattern in the Cu-Cl perovskite is similar to that found in the Pb-Br perovskite.[35]

At room temperature, both $(PED)CuCl_4$ and $(BED)_2CuCl_6$ crystals exhibit yellowish color. Figure 2 shows the temperature-dependent optical micrographs of
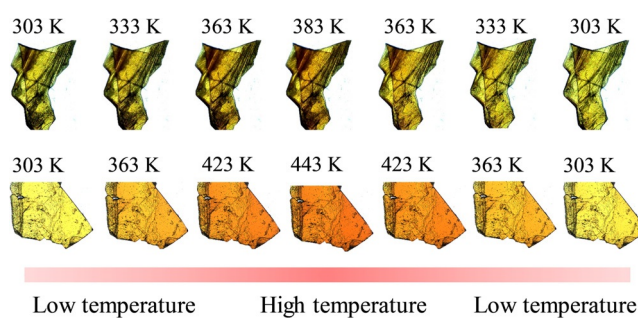

Figure 2. Temperature-induced color change in $(PED)CuCl_4$ crystal (top) and $(BED)_2CuCl_6$ (bottom).

the two typical crystals. Upon temperature rise, the $(PED)CuCl_4$ crystal shows a color change from yellow to slightly dark brown. In contrast, the $(BED)_2CuCl_6$ exhibits more significant color evolution under different temperatures. Upon increasing the temperature from 303 K to 443 K, the crystal color changes from translucent yellow to red-brown. The darkening of the crystal color indicates a reduction in the band gap. Notably, this transition is completely reversible as the red-brown color reverts to translucent yellow upon cooling. Two movies of the reversible thermochromic process are presented in Supporting Information (Movie 1 and Movie 2). Reversible thermochromism in $(BED)_2CuCl_6$ would significantly beneficial to future thermal sensor applications. It is noted that the working temperature of the $(BED)_2CuCl_6$ crystal is the highest in the ever reported thermochromic 2D hybrid perovskite materials. Figure S3 shows the recent progress on representative thermochromic
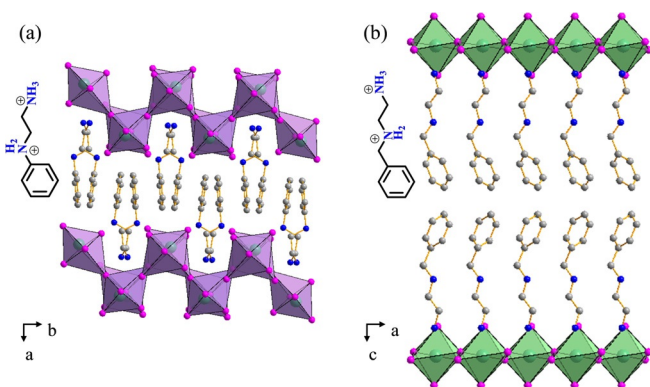

Figure 1. Crystal structures of $(PED)CuCl_4$[51] (a), $(BED)_2CuCl_6$[51] (b). Green Cu, red-brown Cl, blue N, gray C. H atoms are omitted for clarity.

materials, with their highest working temperatures. $(BED)_2CuCl_6$ possess a particularly high thermochromic response temperature in all the reported materials.

Ultraviolet-visible (UV/Vis) absorption spectra were collected for the heating/cooling cycle of $(PED)CuCl_4$ and $(BED)_2CuCl_6$ (Figure S4,S5). When heated to the temperatures of 303 K, 333 K, 363 K, and 383 K, the absorption edges of the $(PED)CuCl_4$ were observed at 596 nm, 613 nm, 635 nm, and 659 nm, respectively. For $(BED)_2CuCl_6$, the absorption edges were observed at 574 nm, 617 nm, 659 nm, and 677 nm, upon heating to 303 K, 363 K, 423 K, and 443 K, respectively. The red shift of the absorption edge with the temperature rise confirms the chromatic variation of the samples.[36] By extrapolating the linear region of the absorption edge to the energy-axis intercept, we have determined the optical band gaps of the two crystals. For $(PED)CuCl_4$, the band gap changed from 2.08 eV to 1.88 eV when the temperature varied from 303 K to 383 K. In comparison, the band gap of the $(BED)_2CuCl_6$ reduced from 2.16 eV to 1.83 eV, when the temperature varied from 303 K to 443 K (Figure S6,S7). This band gap narrowing is consistent with the observed color changes at different temperatures.

As discussed above, the increase in temperature leads to a deepening of $(PED)CuCl_4$ and $(BED)_2CuCl_6$ crystal color, suggesting crystal structure change. Temperaturedependent PXRD patterns were recorded to study the crystal structural changes. Manual grinding powder of $(PED)CuCl_4$ and $(BED)_2CuCl_6$ from the centimeter-sized crystal was used to perform the PXRD measurements. For $(BED)_2CuCl_6$, the powder was heated from 303 K to 423 K and then cooled back to 303 K (see Figure S8 in the Supporting Information for full range diffractograms). Figure 3a shows that the diffraction peak at $2\theta = 41.27°$ shifts to lower 2θ angles ($2\theta = 41.12°$ at 423 K) upon increasing temperature, which gradually shifts back toward higher 2θ angles during the cooling process. The structural evolution of the powder upon heating and cooling is visualized in Figure 3b by comparing the lattice spacing
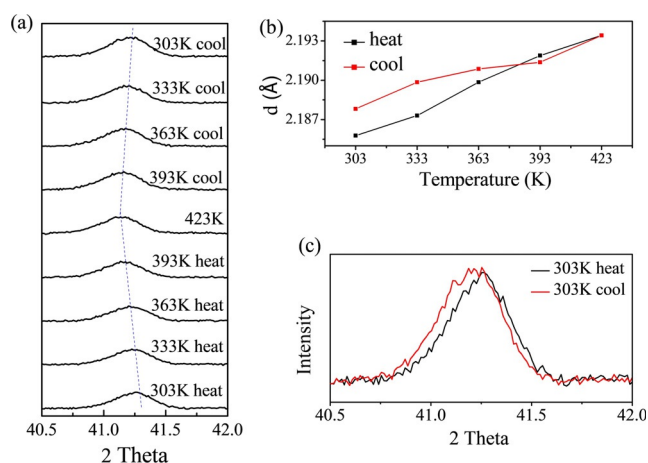
parameter d at each temperature. The results show that d increased with increasing temperature and decreased with decreasing temperature, showing a reversible process. Notably, after one heating and cooling cycle, the peak position did not fully recover to its original position, indicating slight hysteresis (Figure 3c). Similar hysteresis phenomena have been previously reported on 3D $MAPbI_3$ perovskite.[37] Temperature-dependent PXRD measurement on the powder of the $(PED)CuCl_4$ are provided in Figure S9 and Figure S10, which exhibit very similar behavior as that of the $(BED)_2CuCl_6$.

Differential scanning calorimetry (DSC) analysis from 290 K to 380 K for $(PED)CuCl_4$ indicates that no structural phase transition occurs up to the decomposition (Figure S11).[38, 39] To understand the mechanisms of the thermochromism in $(PED)CuCl_4$ and $(BED)_2CuCl_6$ perovskites, we performed single-crystal X-ray structures at 150, 200, 300, and 380 K. For $(PED)CuCl_4$, all structures were solved in the monoclinic space group $P2_1/c$. When the temperature changed from 150 K to 380 K, crystallographic data and refinement parameters show several important changes of the crystal structures. First, the Cu—Cl^1 bond length (see Figure S12 for atom numbering scheme) elongates from 2.2348 Å to 2.2375 Å (Figure S12b), while the other Cu—Cl bonds show a trend of decrease (Table S3) over the same temperature range. Second, the in-plane Cl-Cu-Cl angle[25] (i.e., in-plane buckling of the octahedra, $\theta_{in-plane}$) decreases from 97.17° to 97.00° (Figure S12c). Third, based on the SCXRD measurements, we have also calculated the cell volumes of $(PED)CuCl_4$ at different temperatures (Figure S12d). A linear increase of the cell volume from the 1276.35 Å^3 to 1307.77 Å^3 was obtained, which indicates thermal-induced lattice expansion, consistent with the results from the temperature-dependent PXRD measurements. The gradual lattice expansion with increasing temperature is also consistent with that observed by DSC, which show no thermal anomaly in the temperature range of 290 K to 380 K (Figure S11). The result that only lattice expansion takes place in the crystal, while no structural phase transition occurred, explains the excellent reversibility of the thermochromism in the two-dimensional hybrid perovskites. The DSC and temperature-dependent SCXRD results on the $(BED)_2CuCl_6$ are provided in Figure S11 and Table S2, which exhibit very similar behavior as that of the $(PED)CuCl_4$.

We measured the current–voltage curves of these two perovskite materials as a function of temperature. The representative current–voltage traces of these crystals are provided in Figure 4a, b, which were used in determining the conductivity. These traces are linear at low bias, which suggests Ohmic contact between electrodes and the various crystals.[32] Both crystals show a general trend that their conductivities increase with rising temperature. Figure 4c, d show the conductivity of $(PED)CuCl_4$ and $(BED)_2CuCl_6$ from room temperature to their decomposition temperatures, which illustrate that the conductivity increases significantly as the temperature increase, verifying semiconductor behaviors of both crystals. The electrical conductivity of $(PED)CuCl_4$ increases from 3.51×10^{-10} S cm^{-1} at 303 K to 2.14×10^{-9} S cm^{-1} at 363 K, while $(BED)_2CuCl_6$ increases from

Figure 3. Temperature-dependent PXRD patterns of $(BED)_2CuCl_6$. a) Expansion of the $2\theta = 41.27°$ reflection at different temperatures. b) Lattice spacing calculated from the 2θ values extracted from the PXRD spectra at different temperatures. c) The spectra at $2\theta = 41.27°$ during the heating and cooling cycles.
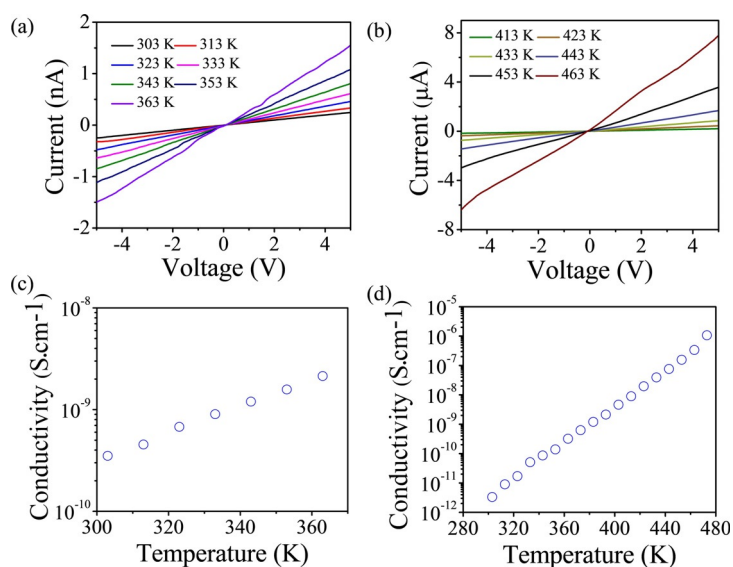
Figure 4. Representative temperature dependence of current–voltage curves on a single-crystal device of (PED)CuCl$_4$ (a), or (BED)$_2$CuCl$_6$ (b) between −5 V and 5 V bias. The plot of conductivity versus temperature for (PED)CuCl$_4$ (c), or (BED)$_2$CuCl$_6$ (d) at 5 V bias.

3.32×10^{-12} S cm^{-1} at 303 K to 1.07×10^{-6} S cm^{-1} at 473 K. Under the same temperature of 363 K, the (PED)CuCl$_4$ possesses a conductivity of 2.14×10^{-9} S cm^{-1}, which is nearly one order of magnitude higher than that of (BED)$_2$CuCl$_6$ (3.19×10^{-10} S cm^{-1}). Importantly, the process of conductivity changed with temperature is reversible, the conductivity is reduced when the temperature is lowered (Figure S13). In previous work, researchers have tried to tune the conductivity of perovskite via changing the organic moieties, and obtained conductivity change can only cover no more than four orders of magnitude.[40,41] In comparison, the conductivity change of (BED)$_2$CuCl$_6$ spans close to six orders of magnitude, which is the highest value for perovskite materials. The reversible and significant conductivity response to temperature makes (BED)$_2$CuCl$_6$ an excellent candidate for thermal sensing applications.

The temperature-dependent conductivity change suggests a thermally activated charge transport mechanism. Fitting the conducting data to the Arrhenius equation $\sigma = \sigma_0 \exp(-E_a/k_B T)$[42,43] can give the activation energy (E_a) of the materials for charge transport, where σ is the electrical conductivity, σ_0 is a prefactor, k_B is the Boltzmann constant, and T is the absolute temperature. We obtained an E_a of 299 meV for the (PED)CuCl$_4$ (Figure S14). In comparison, the E_a of (BED)$_2$CuCl$_6$ is estimated to be 960 meV. In 2D perovskites, the organic cations are considered as insulating groups between the conductive inorganic layers.[44] The activation energy for charge transport in 2D hybrid perovskites is affected by the distance of two adjacent inorganic layers.[25,40] From single crystal structure (Figure S15), the distance between adjacent inorganic layers of these two crystals were 9.672 Å and 24.038 Å, respectively. The reduced activation energy

for charge transport in (PED)CuCl$_4$ compared to (BED)$_2$CuCl$_6$ can be attributed to the shorter distance between adjacent inorganic layers. Therefore, the significantly different conductivity of the two materials can be attribute to their difference in crystal structures, particularly the different distance between the inorganic layers.

Magnetization measurements were performed with a Quantum Design superconducting quantum interference device (SQUID) magnetometer. Temperature-dependent magnetization in a 100 Oe magnetic field for the (PED)CuCl$_4$ and (BED)$_2$CuCl$_6$ show clearly the transition from ferromagnet to paramagnet (Figure 5a,b). The observed rise in magnetization as the temperature decreases are characteristics of the temperature dependence of the magnetization of a ferromagnetic substance.[45,46] Long-range ferromagnetic orders for the (PED)CuCl$_4$ and (BED)$_2$CuCl$_6$ are below 13 K. The Curie temperatures of these two 2D perovskites are similar to that observed on CuCl$_4$(C$_6$H$_5$CH$_2$CH$_2$NH$_3$)$_2$.[47] The ferromagnetic hysteresis loops for the two hybrid perovskites below the Curie temperature are shown in Figure 5c,d. For (PED)CuCl$_4$, the magnetization nearly saturates at a value of 0.12 emu g^{-1} in a field of 2000 Oe at 2 K. However, (BED)$_2$CuCl$_6$ on the other hand, has strong ferromagnetism. The magnetization nearly saturates at a value of 10 emu g^{-1} in a field of 2000 Oe at 2 K. The saturated magnetization of (BED)$_2$CuCl$_6$ is comparable to the value reported in the literature.[32]

The different values of saturated magnetization for (PED)CuCl$_4$ and (BED)$_2$CuCl$_6$ indicate that the magnetic properties of organic–inorganic hybrid perovskite materials are modulated by the organic cations. In organic–inorganic perovskite hybrids, magnetism originates mainly from the transition metal ions, as for these two compounds, from the
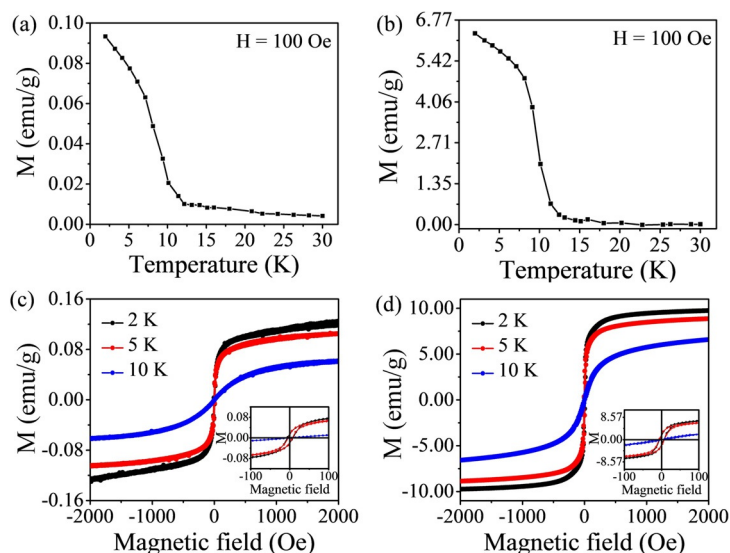

Figure 5. Temperature dependence of the magnetizations of (PED)CuCl$_4$ (a) and (BED)$_2$CuCl$_6$ (b) in applied fields of 100 Oe. The hysteresis loops of (PED)-CuCl$_4$ (c) and (BED)$_2$CuCl$_6$ (d) at 2 K, 5 K, 10 K.

Cu^{2+} ion.[48] The orbitals on neighboring Cu^{2+} ions are orthogonal to each other, and the spins experience ferromagnetic superexchange via a 180° Cu-Cl-Cu pathway.[34] The interaction (so-called superexchange interaction) between the two magnetic Cu^{2+} ions is mediated by the non-magnetic chlorine ion, and this interaction plays an important role in the magnetic properties. It is known that the Cu^{2+} ions in the perovskite structure are strongly Jahn-Teller active, giving rise to changes in the Cu−Cl bond lengths and hence to structural distortions of the $CuCl_6$ octahedra.[49] We quantitatively measure the magnitude of the distortion of the octahedra (Δd) using Equation (1):

$$\Delta d = \frac{1}{6} \sum \left[\frac{d_n - d}{d} \right]^2 \tag{1}$$

where d is the mean Cu−Cl bond length and d_n are the six individual Cu−Cl bond length.[50] In Table S4, the distortions of $CuCl_6$ octahedral in the perovskite structure are listed. The values of Δd is calculated to be 7.022×10^{-2} and 3.904×10^{-6} for the $(PED)CuCl_4$ and $(BED)_2CuCl_6$, respectively. The results suggest that $CuCl_6$ octahedron is significantly distorted with Cu atoms deviating from the balanced sites. Meanwhile, the octahedron in $(PED)CuCl_4$ is much more distorted than $(BED)_2CuCl_6$. On the other hand, unlike the flat $CuCl_6$ layer in the $(BED)_2CuCl_6$, the inorganic layer of $(PED)CuCl_4$ has a corrugated $CuCl_6$ layer (Figure 1). More distorted octahedron and corrugated $CuCl_6$ layer cause the intensity of the superexchange interaction between Cu^{2+} ion in $(PED)CuCl_4$ to be less than that in $(BED)_2CuCl_6$, further leading to weak ferromagnetism.

In summary, we have synthesized two new 2D layered organic–inorganic hybrid perovskites, $(PED)CuCl_4$ and $(BED)_2CuCl_6$, which exhibit reversible thermochromic behavior, dramatic temperature-dependent conductivity change, and strong ferromagnetism. The $(BED)_2CuCl_6$ exhibits a reversible color change from translucent yellow to red-brown as the temperature varies from 303 K to 443 K. A six orders of magnitude change in conductivity of $(BED)_2CuCl_6$ was obtained in the temperature-dependent conductivity measurement, which is the largest conductivity change among perovskite materials reported. Magnetization measurements showed that the $(PED)CuCl_4$ and $(BED)_2CuCl_6$ are both ferromagnetic substance with ferromagnetic ordering below 13 K. The combination of thermochromism with ferromagnetism promises new multifunctional perovskites for potential applications in the optoelectronic and sensing devices.

Acknowledgements

Conflict of interest

The authors declare no conflict of interest.

[1] F. Bella, G. Griffini, J.-P. Correa-Baena, G. Saracco, M. Grätzel, A. Hagfeldt, S. Turri, C. Gerbaldi, *Science* **2016**, *354*, 203–206.

[2] G. E. Eperon, T. Leijtens, K. A. Bush, R. Prasanna, T. Green, J. T.-W. Wang, D. P. McMeekin, G. Volonakis, R. L. Milot, R. May, A. Palmstrom, D. J. Slotcavage, R. A. Belisle, J. B. Patel, E. S. Parrott, R. J. Sutton, W. Ma, F. Moghadam, B. Conings, A. Babayigit, H.-G. Boyen, S. Bent, F. Giustino, L. M. Herz, M. B. Johnston, M. D. McGehee, H. J. Snaith, *Science* **2016**, *354*, 861–865.

[3] C. Cho, S.-H. Jeong, M.-H. Park, Y.-H. Kim, C. Wolf, C.-L. Lee, J. H. Heo, A. Sadhanala, N. Myoung, S. Yoo, S. H. Im, R. H. Friend, T.-W. Lee, *Science* **2015**, *350*, 1222–1225.

[4] Y. Liu, Y. Zhang, Z. Yang, H. Ye, J. Feng, Z. Xu, X. Zhang, R. Munir, J. Liu, P. Zuo, Q. Li, M. Hu, L. Meng, K. Wang, D.-M. Smilgies, G. Zhao, H. Xu, Z. Yang, A. Amassian, J. Li, K. Zhao, S. F. Liu, *Nat. Commun.* **2018**, *9*, 5302.

[5] H. Zhu, Y. Fu, F. Meng, X. Wu, Z. Gong, Q. Ding, M. V. Gustafsson, M. T. Trinh, S. Jin, X.-Y. Zhu, *Nat. Mater.* **2015**, *14*, 636–642.

[6] A. Fu, P. Yang, *Nat. Mater.* **2015**, *14*, 557–558.

[7] B. Saparov, D. B. Mitzi, *Chem. Rev.* **2016**, *116*, 4558–4596.

[8] O. Nazarenko, M. R. Kotyrba, S. Yakunin, M. Aebli, G. Rainò, B. M. Benin, M. Wörle, M. V. Kovalenko, *J. Am. Chem. Soc.* **2018**, *140*, 3850–3853.

[9] L. Mao, P. Guo, M. Kepenekian, I. Hadar, C. Katan, J. Even, R. D. Schaller, C. C. Stoumpos, M. G. Kanatzidis, *J. Am. Chem. Soc.* **2018**, *140*, 13078–13088.

[10] Z. Wu, X. Liu, C. Ji, L. Li, S. Wang, Y. Peng, K. Tao, Z. Sun, M. Hong, J. Luo, *J. Am. Chem. Soc.* **2019**, *141*, 3812–3816.

[11] W.-Q. Liao, D. Zhao, Y.-Y. Tang, Y. Zhang, P.-F. Li, P.-P. Shi, X.-G. Chen, Y.-M. You, R.-G. Xiong, *Science* **2019**, *363*, 1206–1210.

[12] X. Li, J. Hoffman, W. Ke, M. Chen, H. Tsai, W. Nie, A. D. Mohite, M. Kepenekian, C. Katan, J. Even, M. R. Wasielewski, C. C. Stoumpos, M. G. Kanatzidis, *J. Am. Chem. Soc.* **2018**, *140*, 12226–12238.

[13] Y. Tian, C. Zhou, M. Worku, X. Wang, Y. Ling, H. Gao, Y. Zhou, Y. Miao, J. Guan, B. Ma, *Adv. Mater.* **2018**, *30*, 1707093.

[14] Y. Zhang, P. Wang, M. C. Tang, D. Barrit, W. Ke, J. Liu, T. Luo, Y. Liu, T. Niu, D. M. Smilgies, Z. Yang, Z. Liu, S. Jin, M. G. Kanatzidis, A. Amassian, S. F. Liu, K. Zhao, *J. Am. Chem. Soc.* **2019**, *141*, 2684–2694.

[15] J. Chen, Y. Wang, L. Gan, Y. He, H. Li, T. Zhai, *Angew. Chem. Int. Ed.* **2017**, *56*, 14893–14897; *Angew. Chem.* **2017**, *129*, 15089–15093.

[16] F. O. Saouma, C. C. Stoumpos, J. Wong, M. G. Kanatzidis, J. I. Jang, *Nat. Commun.* **2017**, *8*, 742.

[17] J. Hu, I. W. H. Oswald, S. J. Stuard, M. M. Nahid, N. Zhou, O. F. Williams, Z. Guo, L. Yan, H. Hu, Z. Chen, X. Xiao, Y. Lin, Z. Yang, J. Huang, A. M. Moran, H. Ade, J. R. Neilson, W. You, *Nat. Commun.* **2019**, *10*, 1276.

[18] H. Lu, X. Chen, J. E. Anthony, J. C. Johnson, M. C. Beard, *J. Am. Chem. Soc.* **2019**, *141*, 4919–4927.

[19] H. Hu, F. Meier, D. Zhao, Y. Abe, Y. Gao, B. Chen, T. Salim, E. E. M. Chia, X. Qiao, C. Deibel, Y. M. Lam, *Adv. Mater.* **2018**, *30*, 1707621.

[20] I. V. Kabakova, I. Azuri, Z. Chen, P. K. Nayak, H. J. Snaith, L. Kronik, C. Paterson, A. A. Bakulin, D. A. Egger, *J. Mater. Chem. C* **2018**, *6*, 3861–3868.

[21] W. Xu, L. Zheng, X. Zhang, Y. Cao, T. Meng, D. Wu, L. Liu, W. Hu, X. Gong, *Adv. Energy Mater.* **2018**, *8*, 1703178.

[22] J. Huang, M. Lai, J. Lin, P. Yang, *Adv. Mater.* **2018**, *30*, 1802856.

[23] Y. Shi, Z. Ma, D. Zhao, Y. Chen, Y. Cao, K. Wang, G. Xiao, B. Zou, *J. Am. Chem. Soc.* **2019**, *141*, 6504–6508.

[24] T. Yin, B. Liu, J. Yan, Y. Fang, M. Chen, W. K. Chong, S. Jiang, J.-L. Kuo, J. Fang, P. Liang, S. Wei, K. P. Loh, T. C. Sum, T. J. White, Z. X. Shen, *J. Am. Chem. Soc.* **2019**, *141*, 1235–1241.

[25] A. Jaffe, Y. Lin, W. L. Mao, H. I. Karunadasa, *J. Am. Chem. Soc.* **2015**, *137*, 1673–1678.

[26] Y. Yuan, X.-F. Liu, X. Ma, X. Wang, X. Li, J. Xiao, X. Li, H.-L. Zhang, L. Wang, *Adv. Sci.* **2019**, *6*, 1900240.

[27] A. Halder, D. Choudhury, S. Ghosh, A. S. Subbiah, S. K. Sarkar, *J. Phys. Chem. Lett.* **2015**, *6*, 3180–3184.

[28] N. Wang, L. Cheng, R. Ge, S. Zhang, Y. Miao, W. Zou, C. Yi, Y. Sun, Y. Cao, R. Yang, Y. Wei, Q. Guo, Y. Ke, M. Yu, Y. Jin, Y. Liu, Q. Ding, D. Di, L. Yang, G. Xing, H. Tian, C. Jin, F. Gao, R. H. Friend, J. Wang, W. Huang, *Nat. Photonics* **2016**, *10*, 699–704.

[29] W. Zou, R. Li, S. Zhang, Y. Liu, N. Wang, Y. Cao, Y. Miao, M. Xu, Q. Guo, D. Di, L. Zhang, C. Yi, F. Gao, R. H. Friend, J. Wang, W. Huang, *Nat. Commun.* **2018**, *9*, 608.

[30] C. Katan, N. Mercier, J. Even, *Chem. Rev.* **2019**, *119*, 3140–3192.

[31] B. Vargas, R. Torres-Cadena, J. Rodríguez-Hernández, M. Gembicky, H. Xie, J. Jiménez-Mier, Y.-S. Liu, E. Menéndez-Proupin, K. R. Dunbar, N. Lopez, P. Olalde-Velasco, D. Solis-Ibarra, *Chem. Mater.* **2018**, *30*, 5315–5321.

[32] B. Huang, J.-Y. Zhang, R.-K. Huang, M.-K. Chen, W. Xue, W.-X. Zhang, M.-H. Zeng, X.-M. Chen, *Chem. Sci.* **2018**, *9*, 7413–7418.

[33] G. Long, C. Jiang, R. Sabatini, Z. Yang, M. Wei, L. N. Quan, Q. Liang, A. Rasmita, M. Askerka, G. Walters, X. Gong, J. Xing, X. Wen, R. Quintero-Bermudez, H. Yuan, G. Xing, X. R. Wang, D. Song, O. Voznyy, M. Zhang, S. Hoogland, W. Gao, Q. Xiong, E. H. Sargent, *Nat. Photonics* **2018**, *12*, 528–533.

[34] D. I. Khomskii, K. I. Kugel, *Solid State Commun.* **1973**, *13*, 763–766.

[35] L. Mao, Y. Wu, C. C. Stoumpos, M. R. Wasielewski, M. G. Kanatzidis, *J. Am. Chem. Soc.* **2017**, *139*, 5210–5215.

[36] M. De Bastiani, M. I. Saidaminov, I. Dursun, L. Sinatra, W. Peng, U. Buttner, O. F. Mohammed, O. M. Bakr, *Chem. Mater.* **2017**, *29*, 3367–3370.

[37] A. Osherov, E. M. Hutter, K. Galkowski, R. Brenes, D. K. Maude, R. J. Nicholas, P. Plochocka, V. Bulović, T. J. Savenije, S. D. Stranks, *Adv. Mater.* **2016**, *28*, 10757–10763.

[38] W. Ning, X.-G. Zhao, J. Klarbring, S. Bai, F. Ji, F. Wang, S. I. Simak, Y. Tao, X.-M. Ren, L. Zhang, W. Huang, I. A. Abrikosov, F. Gao, *Adv. Funct. Mater.* **2019**, *29*, 1807375.

[39] J. Long, J. Rouquette, J.-M. Thibaud, R. A. S. Ferreira, L. D. Carlos, B. Donnadieu, V. Vieru, L. F. Chibotaru, L. Konczewicz, J. Haines, Y. Guari, J. Larionova, *Angew. Chem. Int. Ed.* **2015**, *54*, 2236–2240; *Angew. Chem.* **2015**, *127*, 2264–2268.

[40] J. V. Passarelli, D. J. Fairfield, N. A. Sather, M. P. Hendricks, H. Sai, C. L. Stern, S. I. Stupp, *J. Am. Chem. Soc.* **2018**, *140*, 7313–7323.

[41] C. Ortiz-Cervantes, P. I. Román-Román, J. Vazquez-Chavez, M. Hernández-Rodríguez, D. Solis-Ibarra, *Angew. Chem. Int. Ed.* **2018**, *57*, 13882–13886; *Angew. Chem.* **2018**, *130*, 14078–14082.

[42] L. S. Xie, L. Sun, R. Wan, S. S. Park, J. A. DeGayner, C. H. Hendon, M. Dincă, *J. Am. Chem. Soc.* **2018**, *140*, 7411–7414.

[43] K. Xu, J. F. Vliem, A. Meijerink, *J. Phys. Chem. C* **2019**, *123*, 979–984.

[44] H. Tsai, W. Nie, J.-C. Blancon, C. C. Stoumpos, R. Asadpour, B. Harutyunyan, A. J. Neukirch, R. Verduzco, J. J. Crochet, S. Tretiak, L. Pedesseau, J. Even, M. A. Alam, G. Gupta, J. Lou, P. M. Ajayan, M. J. Bedzyk, M. G. Kanatzidis, A. D. Mohite, *Nature* **2016**, *536*, 312–316.

[45] W. E. Estes, D. B. Losee, W. E. Hatfield, *J. Chem. Phys.* **1980**, *72*, 630.

[46] H. Pan, Y. Sun, Y. Zheng, N. Tang, Y. Du, *New J. Phys.* **2016**, *18*, 093021.

[47] A. O. Polyakov, A. H. Arkenbout, J. Baas, G. R. Blake, A. Meetsma, A. Caretta, P. H. M. van Loosdrecht, T. T. M. Palstra, *Chem. Mater.* **2012**, *24*, 133–139.

[48] A. Aqeel, N. Akhtar, A. O. Polyakov, P. Rudolf, T. T. M. Palstra, *APL Mater.* **2018**, *6*, 114206.

[49] H. Arend, W. Huber, F. H. Mischgofsky, G. K. R.-V. Leeuwen, *J. Cryst. Growth* **1978**, *43*, 213–223.

[50] J. A. Alonso, M. J. Martínez-Lope, M. T. Casais, *Inorg. Chem.* **2000**, *39*, 917–923.

[51] CCDC CCDC 1964882 ((PED)CuCl₄) and 1964883 ((BED)₂CuCl₆) contain the supplementary crystallographic data for this paper. These data can be obtained free of charge from The Cambridge Crystallographic Data Centre.